Optica Applicata, Vol. LII, No. 2, 2022
DOI: 10.37190/oa220211

Broadband convolutional scattering characteristics of all dielectric transmission Pancharatnam–Berry geometric phase metasurfaces

YIYUN LI[1, 2], YONGXING JIN[1,*], XUFENG JING[1, 2], LIJIANG SHI[3], CHENXIA LI[1], ZHI HONG[2]

[1]Institute of Optoelectronic Technology, China Jiliang University, Hangzhou 310018, China

[2]Centre for THz Research, China Jiliang University, Hangzhou 310018, China

[3]Hangzhou Hangxin Qihui Technology Co., Ltd, Hangzhou, China

[*]Corresponding author: jinyongxing@cjlu.edu.cn

In order to obtain the broadband scattering characteristics, we propose a superperiodic cell structure with all-dielectric material to construct Pancharatnam–Berry geometric phase encoding metasurfaces. Because we cannot design or prepare infinitesimal coding unit particles, according to the generalized Snell's law, we can only obtain discrete scattering angle regulation for the basic coding metasurface sequence. In order to obtain multi-angle scattering characteristics, we introduce the Fourier convolution principle in digital signal processing on the Pancharatnam–Berry geometric phase encoding metasurfaces. By using the addition and subtraction operations on two encoding metasurface sequences, a new encoding metasurface sequence can be obtained with different deflection angle. Fourier convolution operations on the encoding metasurfaces can provide an efficient method in optimizing encoding patterns to achieve continuous scattering beams. The addition and subtraction methods are also applicable to the checkerboard coding mode. The combination of Fourier convolution principle and Pancharatnam–Berry phase coded metasurface in digital signal processing can realize more powerful electromagnetic wave manipulation capability.

Keywords: grating, metasurface, optics devices.

1. Introduction

The metasurface can be regarded as the two-dimensional corresponding structure of the metamaterial, which is an artificial layered anisotropic quasi-periodic structure array with a wavelength smaller than the thickness [1–10]. Metasurfaces have some extraordinary physical properties that are not found in materials in nature [11–25]. Recently, CUI *et al*. putted forward the new concept of "encoding metamaterials" [26], and briefly described the related methods of programmable metamaterials. Also, the concept of encoding metasurface began to capture people's attention. For example, it can flexibly and efficiently change the characteristics of electromagnetic wave amplitude, phase, propagation mode and other aspects [27–39]. At the same time, it also has the advantages of simple preparation process, large-scale integration, low loss, *etc*., which also makes encoding metasurfaces have broad application prospects in the fields of holographic imaging [27], vortex beam generation [16, 17], and stealth technology.

The early research on encoding metasurfaces was basically focused on the resonance phase metasurfaces, which changed the resonance frequency through structural changes, thereby changing the phase of a certain frequency point, resulting in phase mutations. The use of resonant phase encoding metasurfaces can realize some basic electromagnetic wave control methods, such as deflection, focusing, and polarization conversion [14–18]. However, the resonant phase encoding metasurfaces have also led to some defects, such as high requirements for machining accuracy, small differences in the size of the structure, and limited bandwidth [27]. In order to solve these defects, another type of Pancharatnam–Berry geometric phase encoding metasurface was proposed. The Pancharatnam–Berry geometric phase metasurface is composed of several identical structures with different rotation angles [40]. The condition for achieving phase mutation is to change the rotation angle of the structure, thus greatly reducing the requirements on the processing technology. At the same time, it can also achieve electromagnetic wave control phenomena such as holographic imaging and special beam excitation. It can be said that the emergence of Pancharatnam–Berry geometric phase encoding metasurfaces gives us more freedom to manipulate electromagnetic waves. However, initial studies of Pancharatnam–Berry coded metasurface focused on metal structures. The ohmic loss of metal materials seriously affects the efficiency of coded metasurface devices, especially, for visible light region. Here, we propose to control the scattering characteristics of electromagnetic waves by using all dielectric Pancharatnam–Berry coded metasurface. A superlattice structure with the cell structure containing two substructures is proposed to further realize the wideband manipulation of electromagnetic waves in the visible band.

The Pancharatnam–Berry geometric phase metasurface is composed of discrete unit structures [41], and the size of a unit structure cannot be designed to be infinitesimal. According to the generalized Snell's law [42,43], the deflection angle of the electromagnetic wave depends on the size of the unit structure. However, according to the distribution characteristics of the coded metasurface unit structure, the deflection angle of the electromagnetic wave can only be limited. That is to say, for ordinary code metasurface, it is impossible to realize continuous variation of the deflection angle of electromagnetic wave. In order to realize the continuous regulation of incident electromagnetic wave by Pancharatnam–Berry phase coded metasurface, we introduce the principle of Fourier convolution in digital signal processing on Pancharatnam–Berry phase coded metasurface. By adding and subtracting different coded metasurface sequences, one can get more and even more continuous far field deflections.

2. Far field scattering of encoding metasurface

Generally, encoding metasurfaces are mainly divided into 1-bit, 2-bit and 3-bit metasurfaces. The 1-bit encoding metasurface is composed of two units with a 180° phase

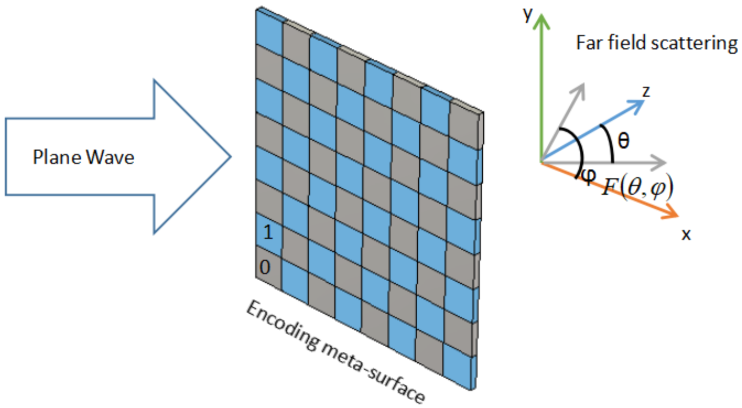

Fig. 1. Schematic diagram of coding metasurface principle.

difference, corresponding to binary numbers 0 and 1, respectively. The 2-bit encoding metasurface is composed of four units with phases of 0°, 90°, 180°, 270°, corresponding to binary numbers 00, 01, 10, 11. The 3-bit and higher bits coding metasurface are composed of more units in the phase range of 0 to 2π. As shown in Fig. 1, the blue grid and gray grid represent the unit of 1 and 0, respectively. Assuming that the transmission phase of the unit (m, n) is $\varphi(m, n)$, when a plane wave is incident perpendicularly on an encoding metasurface, the far-field transmission of the surface can be expressed as [26]

$$F(\theta, \varphi) = f_{\mathrm{e}}(\theta, \varphi) \sum_{m=1}^{M} \sum_{n=1}^{N} \exp\left\{-i\varphi(m, n) - ik_0 P \sin\theta \left[\left(m - \frac{1}{2}\right)\cos\varphi + \left(n - \frac{1}{2}\right)\sin\varphi\right]\right\} \tag{1}$$

where the wave vector $k_0 = \lambda/2\pi$, φ is the azimuth, $f_{\mathrm{e}}(\theta, \varphi)$ indicates the radiation direction of the unit structure, and P stands for unit structure size. The above formula can be further simplified to

$$F(\theta, \varphi) = f_{\mathrm{e}}(\theta, \varphi) \sum_{m=1}^{N} \exp\left\{-i\left[\varphi_m + kP\left(m - \frac{1}{2}\right)\sin\theta\cos\varphi\right]\right\} \times \sum_{n=1}^{N} \exp\left\{-i\left[\varphi_n + kP\left(n - \frac{1}{2}\right)\sin\theta\sin\varphi\right]\right\} \tag{2}$$

Here, φ_m is the phase of the horizontal encoding unit; φ_n is the phase of the encoding unit in the vertical direction. From Eqs. (1) and (2), it can be obtained that $\varphi(m, n) = \varphi_m + \varphi_n$.

By using the generalized Snell's law, the elevation angles θ and azimuth angles φ of the scattering beam on the encoded metasurface can be obtained as [26]

$$\theta = \arcsin\frac{\sqrt{(k_0\sin\theta_i\cos\varphi_i + \nabla\varphi_x)^2 + (k_0\sin\theta_i\sin\varphi_i + \nabla\varphi_y)^2}}{k_0} \tag{3}$$

$$\varphi = \pm\arctan\frac{k_0\sin\theta_i\sin\varphi_i + \nabla\varphi_y}{k_0\sin\theta_i\cos\varphi_i + \nabla\varphi_x} \tag{4}$$

where the phase gradient along the x direction can be defined as $\nabla\varphi_x = \mathrm{d}\varphi_x/\mathrm{d}x$, the phase gradient along the y direction can be defined as $\nabla\varphi_y = \mathrm{d}\varphi_y/\mathrm{d}y$, and θ_i and φ_i are the incident angle and azimuth angle of the incident beam, respectively. $\mathrm{d}\varphi_x$ and $\mathrm{d}\varphi_y$ are the phase difference between adjacent elements in the x and y directions, respectively. When an electromagnetic wave is perpendicular to the coded metasurface with the encoding sequence 0101…/0101…, the elevation angle and azimuth angle of scattering beams can be obtained as $\theta = \arcsin(\lambda/2p)$, $\varphi = 0°$, and $\varphi = 180°$, respectively. If the encoding sequence contains n cell structures for the superperiod, the elevation angle can be defined as $\theta = \arcsin(\lambda/nP)$. Therefore, by changing the period length of the gradient sequence, we can change the elevation angle of the scattered beams.

3. Pancharatnam–Berry geometric phase unit structure design of encoding metasurface

Figure 2 shows the unit structure of the metasurface with all dielectric material. The two purple strips on the top are made of TiO_2, and the pink square structure on the bottom is made of SiO_2. Two strips with different lengths are stacked on the base. The surface roughness of titanium dioxide is low, and titanium dioxide has a higher refractive index ($n = 2.4$), dielectric constant $\varepsilon = 5.76$, and magnetic permeability $\mu = 1$, so it can achieve

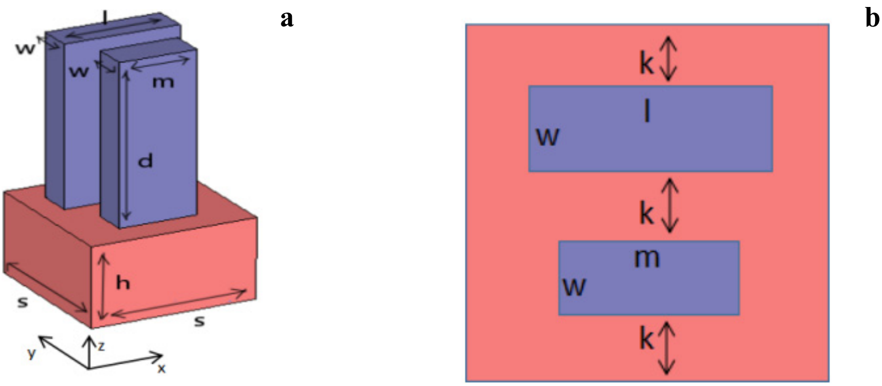

Fig. 2. Schematic diagram of metasurface unit structure.

a higher transmission amplitude ratio, thereby improving the scattering efficiency of the device. As a low-cost and easy-to-obtain material, silicon dioxide also has a high transmittance in the visible light band, and is very suitable as a base material. The geometric parameters of the strip structure are shown in Fig. 2**b** as $W = 95$ nm, $l = 300$ nm, $m = 200$ nm, the height of the strip structure is $d = 600$ nm, the height of the substrate is $h = 300$ nm, and the side length is $S = 430$ nm. It can be seen from the top view that the distance between the two strip structures and the edge of the square structure are both $k = 80$ nm. The length of the strip structure is along the x direction, the width is along the y direction, and the height is along the z direction.

In order to study the transmission characteristics and phase characteristics of the designed unit structure, a finite integral method was used to simulate transmission and scattering characteristics on the coded metasurface. In calculation, the unit cell boundary conditions were set in the x and y direction. The open boundary condition was set in the z direction. The incident wave with TE(0,0) and TM(0,0) modes is incident on the designed units. TE(0,0) mode can be defined as the electric field vector along x direction, and TM(0,0) mode can be defined as the electric field vector along the y direction. The transmission phase and transmission coefficient are demonstrated in Fig. 3. It can be seen that the phases of TE(0,0) and TM(0,0) modes at 555.24THz are –152.6762 and 27.0839, respectively, and the phase difference between the two units is close to π. The transmittances of the two polarization modes are 0.9557 and 0.8699, both of which are relatively high. The characteristics of these phase and transmission coefficients satisfy the Pancharatnam–Berry phase theory. Next, we will rotate the designed cell structure to obtain different phase distributions to construct Pancharatnam–Berry phase coded metasurfaces.

When the unit structure is rotated counterclockwise by 0°, 45°, 90°, 135°, respectively, these four units can be defined as code number 0, 1, 2, and 3, respectively, forming a 2 bit code element surface. When a left-circularly polarized light is incident on the element structure, the transmission phase and transmission coefficient of dextral

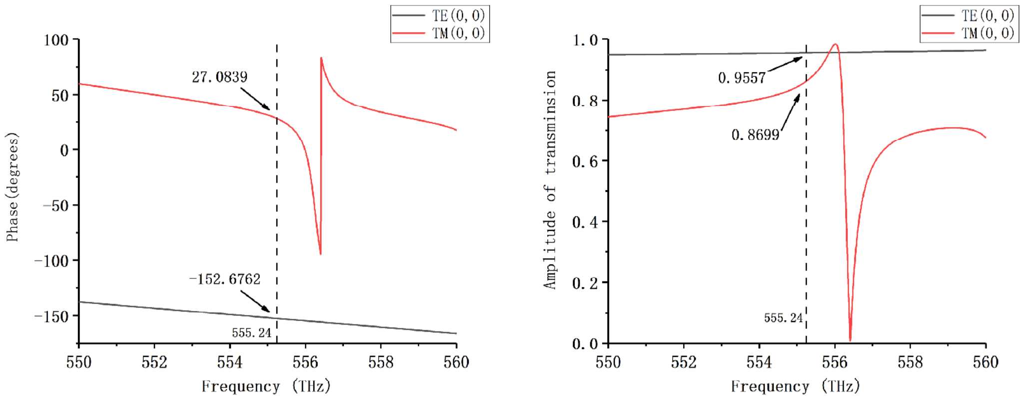

Fig. 3. Transmission phase (**a**) and amplitude (**b**) for TE(0,0) and TM(0,0) modes on the designed unit cell.

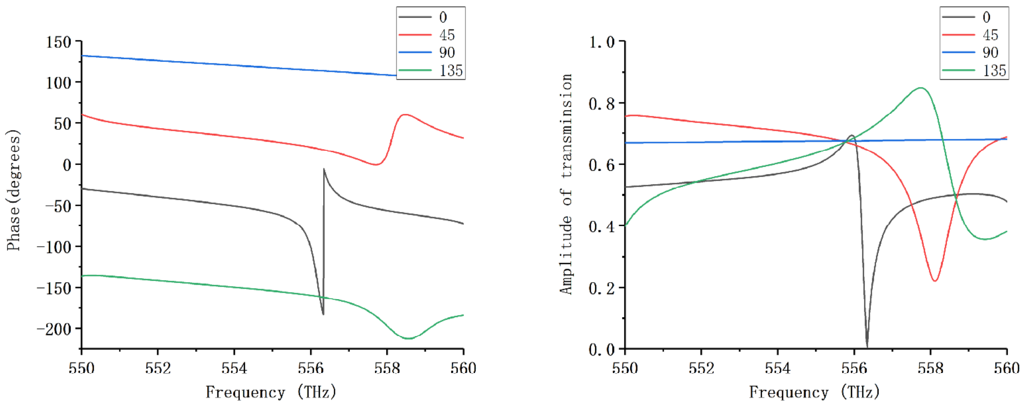

Fig. 4. Transmission phase and transmission coefficient of the four coded particles 0, 1, 2, and 3.

circularly polarized light with cross polarization are shown in Fig. 4. It can be seen that the phase difference between adjacent coded particles is basically 90°, and the transmittance is high, so they can be used as coded particles to construct 2-bit Pancharatnam–Berry phase encoding metasurfaces. The rotation characteristics of the four coded particles are demonstrated in the Table.

T a b l e. Rotation characteristics of the four coded particles at 555.24 THz.

Parameter	Block construction			
	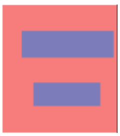			
θ [deg]	0	45	90	135
Code	00\0	01\1	10\2	11\3
Phase	62.623	26.230	117.319	–155.444
Amplitude	0.613	0.687	0.675	0.646

4. Basic sequences of Pancharatnam–Berry phase encoding metasurfaces

Using the above-mentioned 2-bit coded particles, Pancharatnam–Berry phase encoding metasurfaces with different sequences can be constructed. For example, the encoding sequences of S1 (01230123) and S2 (00112233) can be designed with 8 × 8 encoding particles. Also, the sequence S3 (000111222333) was designed with 12 × 12 encoding particles. These phase gradient coded metasurface sequences, such as S1, S2 and S3, may be called basic sequences. Figure 5 shows the arrangement of the basic sequence S1. In the figure, the different color lines with red, yellow, blue, and green,

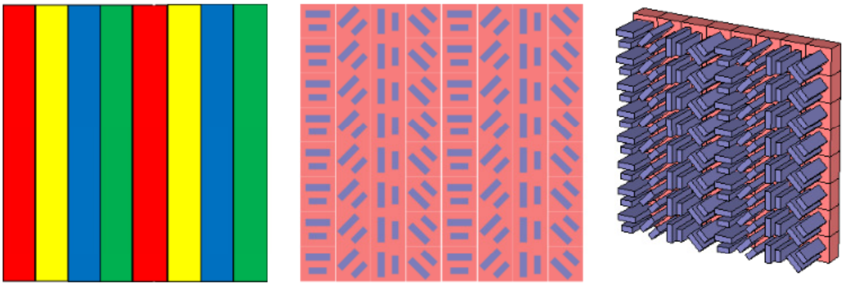

Fig. 5. The arrangement of the basic sequence S1.

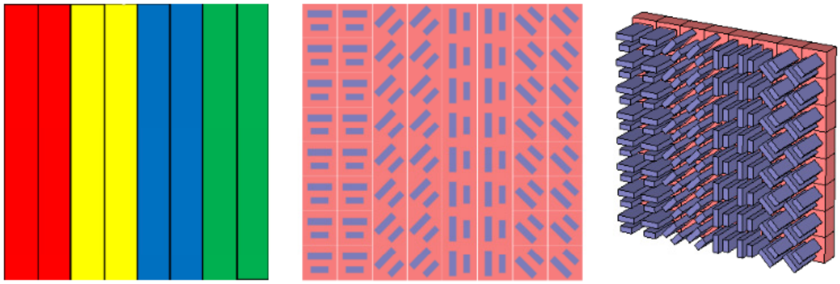

Fig. 6. The arrangement of the basic sequence S2.

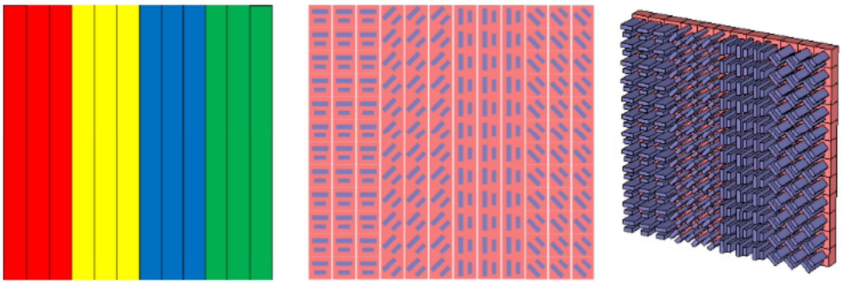

Fig. 7. The arrangement of the basic sequence S3.

respectively, correspond to the four coded particles of 0, 1, 2 and 3. The arrangement of the basic sequences S2 and S3 is shown in Figs. 6 and 7, respectively.

At the base side length of a single particle $S = 430$ nm, the encoding sequence period can be calculated as $\tau_{S1} = 4S = 1720$ nm, $\tau_{S2} = 8S = 3440$ nm, and $\tau_{S3} = 12S = 5160$ nm. According to Eq. (3) and incident wavelength of $\lambda = c/v = 540.31$ nm, the transmission deflection angles for the encoding sequences S1, S2 and S3 can be calculated as $\theta_1 = 18.31°$, $\theta_2 = 9.04°$, and $\theta_3 = 6.01°$. In the simulation, the boundary conditions in the x, y, and z directions on the encoding metasurfaces are set as open conditions to obtain the transmission characteristics of S1, S2, and S3. The corresponding scattering

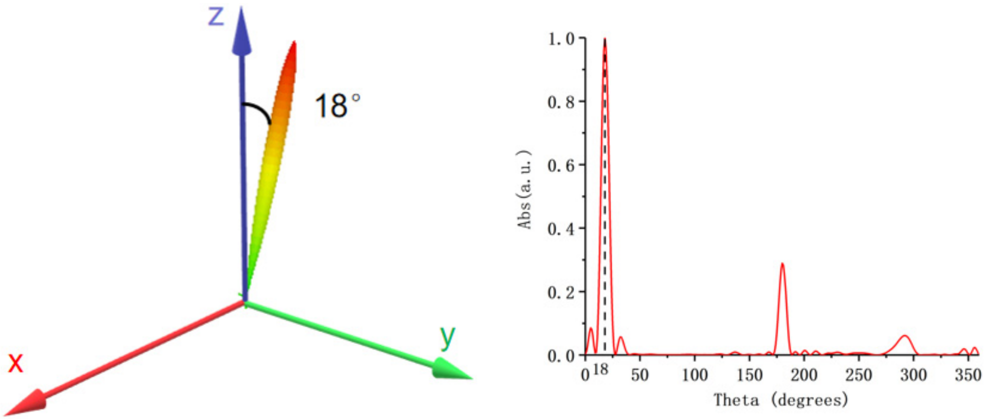

Fig. 8. Scattering angle of the basic sequence S1.

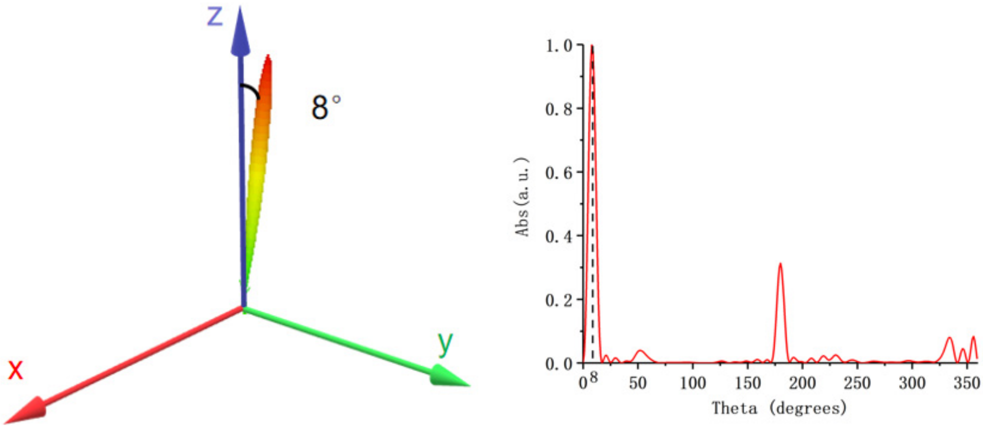

Fig. 9. Scattering angle of the basic sequence S2.

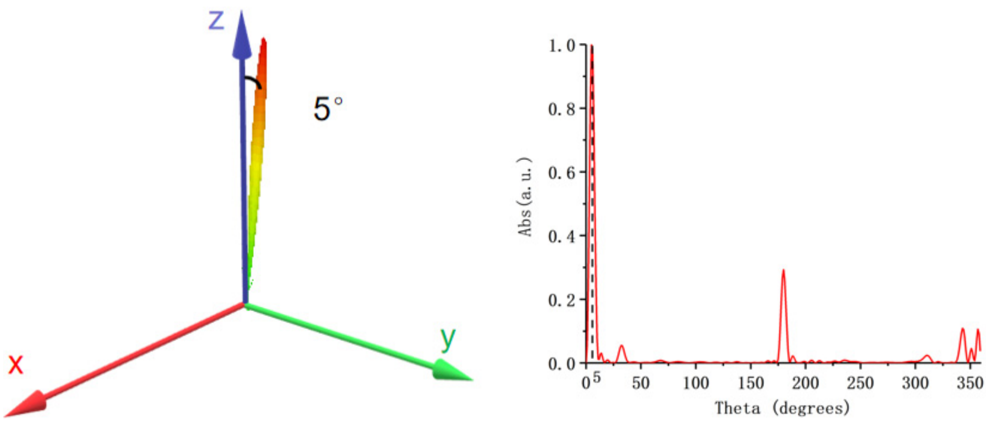

Fig. 10. Scattering angle of the basic sequence S3.

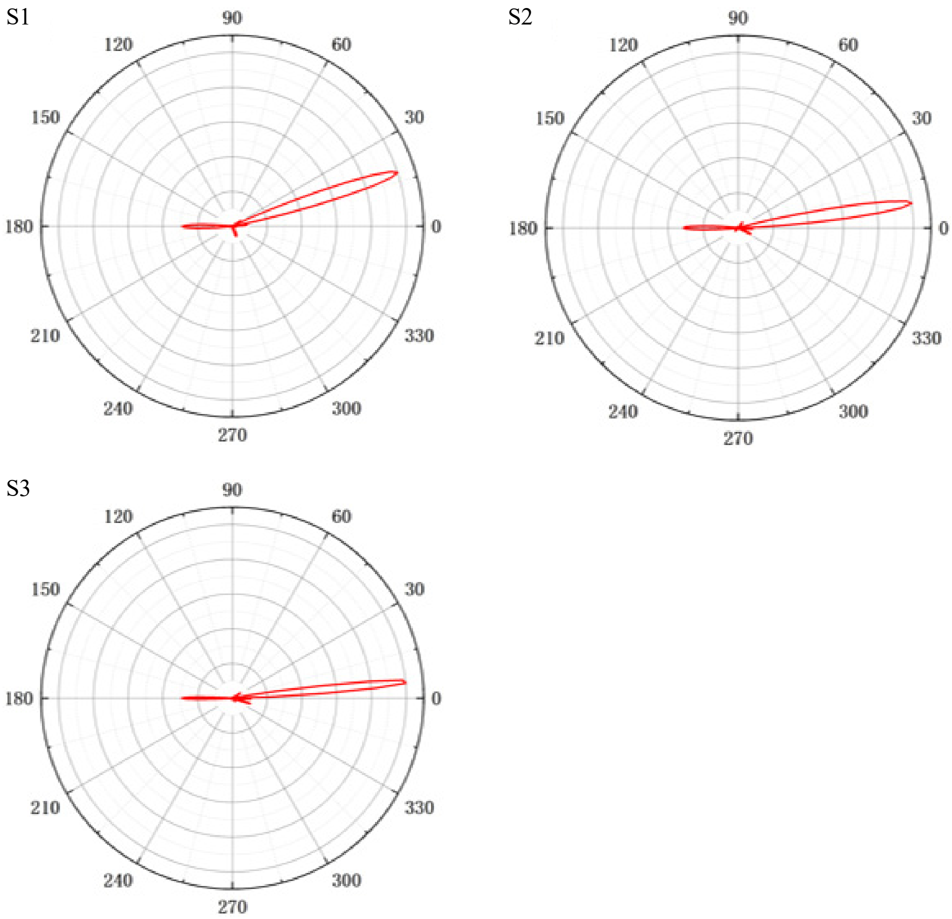

Fig. 11. Polar coordinate scattering of S1, S2, S3.

angles were numerically simulated in Figs. 8, 9 and 10, for S1, S2 and S3, respectively. Also, the polar coordinate scattering is shown in Fig.11. It can be seen that the transmission angles of S1, S2, and S3 are $\theta_1 = 18°$, $\theta_2 = 8°$, and $\theta_3 = 5°$, respectively, which are basically in agreement with the theoretical calculation results. Figure 11 shows the large reflected energy, which is due to the impedance mismatch of the overall planar structure. We can further optimize the structure of these units to achieve impedance matching, thus reducing the reflected energy.

5. Fourier convolution operations of Pancharatnam–Berry phase encoding metasurfaces

According to the encoding sequences S1, S2 and S3, it can be seen that discrete deflection angles of scattering beam are obtained. In order to achieve multi-angle or continuous angle regulation, we will introduce the Fourier convolution theory in digital signal processing to perform addition and subtraction operations on the Pancharatnam–Berry phase encoding metasurfaces. In digital signal processing, the time domain and frequency domain are Fourier transform pairs. They can be represented by mathematical formulas as [26]

$$f(t) \cdot g(t) \overset{\text{FFT}}{\Leftrightarrow} f(\omega) * g(\omega) \tag{5}$$

where t stands for the time domain, and w stands for the frequency domain. Similarly, the near field and far field distributions of the encoding metasurface are also Fourier transform pairs. Therefore, we can compare coded metasurface sequences to time signals, and the far-field scattering angle can be likened to a frequency signal as $t \to x_\lambda = \Gamma/\lambda$ and $t \to \sin\theta$. So, for the encoding metasurfaces, Eq. (5) can be replaced by

$$f(x_\lambda) \cdot g(x_\lambda) \overset{\text{FFT}}{\Leftrightarrow} f(\sin\theta) * g(\sin\theta) \tag{6}$$

where x_λ shows the electrical length. When $g(\omega)$ can be considered as a Dirac-delta function, Eq. (5) can be further simplified as

$$f(t) \cdot g(t)\exp(i\omega_0 t) \overset{\text{FFT}}{\Leftrightarrow} f(\omega) * \delta(\omega - \omega_0) \tag{7}$$

where $\exp(i\omega_0 t)$ stands for the time-shift item in the time domain. Similarly, Eq. (6) can be further deduced as

$$f(x_\lambda) \cdot \exp(i\sin\theta_0\, x_\lambda) \overset{\text{FFT}}{\Leftrightarrow} F(\sin\theta - \sin\theta_0) = F(\sin\theta - \sin\theta_0) \tag{8}$$

where $\exp(i\sin\theta_0 x_\lambda)$ represents a coded sequence with unit amplitude and gradient phase From Eq. (8), it can be understood that the multiplication of a coding metasurface sequence $f(x_\lambda)$ by an encoding sequence $\exp(i\sin\theta_0 x_\lambda)$ leads to a deviation of the scattering pattern away from its original direction by $\sin(\theta_0)$. It should be noted that the scattering angles of the new encoding sequence after Fourier convolution operation cannot be obtained by adding or subtracting the scattering angles of the two encoding sequences. The scattering angle of the new coded sequence should be calculated by

$$\theta' = \sin^{-1}(\sin\theta_1 \pm \sin\theta_2) \tag{9}$$

where θ_1 and θ_2 represent the scattering angles of the two coded metasurface sequences, respectively, and $\sin\theta_1 + \sin\theta_2 < 1$.

According to the above mentioned basic sequences and the Fourier convolution principle, we can get 0 + 0 = 0, 0 + 1 = 1, 0 + 2 = 2, 0 + 3 = 3, 1 + 1 = 2, 1 + 2 = 3, 1 + 3 = 0, 2 + 2 = 0, and 2 + 3 = 1. The new encoding sequence can be obtained by using Fourier convolution operation as S4 = S1 + S2, S5 = S1 + S3, and S6 = S2 + S3. These coding sequences may be referred to as non-basic sequences. After the addition operation of Fourier convolution principle, the new encoding metasurface sequence

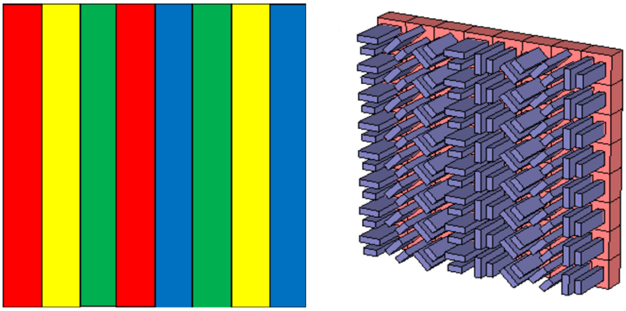

Fig. 12. Arrangement of non-basic sequence S4.

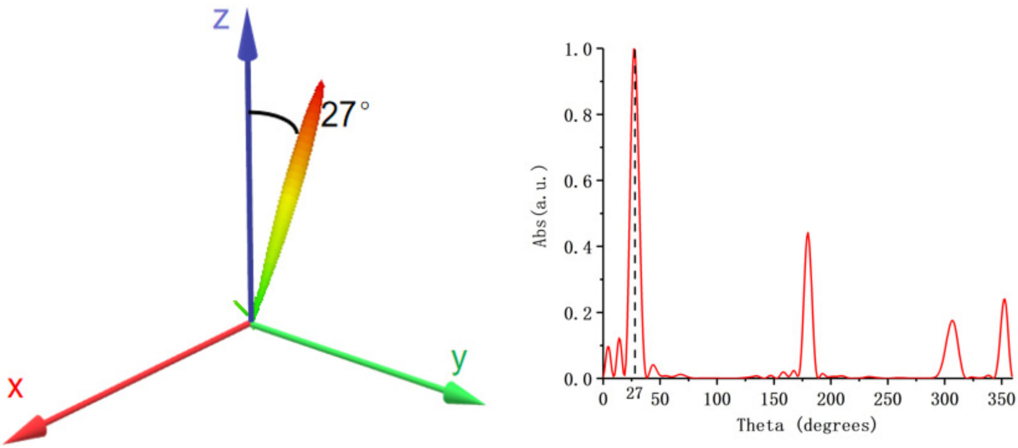

Fig. 13. 3D scattering angle of non-basic sequence S4.

S4 is shown in Fig. 12. S4 = S1 + S2 = 01302312..., and the super-period of encoding sequence is τ_{S4} = 8S = 3440 nm. According to Eq. (9), the theoretical scattering angle of θ_4 can be calculated as $\sin\theta_4 = \lambda/4S + \lambda/8S = 0.4712$, and the θ_4 is 28.11°. The corresponding far field scattering is demonstrated in Fig. 13. It can be seen that the scattering angle can be obtained as $\theta_4 = 27°$. The calculation result is in good agreement with the simulation result.

After the addition operation of the two encoding metasurface sequences of S1 and S3, the new encoding metasurface sequence S5 can be obtained as shown in Fig. 14. S5 = S1 + S3 = 012..., and the super-period of encoding sequence is τ_{S5} = = 3S = 1290 nm. The theoretical scattering angle of θ_5 can be calculated as $\sin\theta_5 = = \lambda/4S + \lambda/12S = 0.4188$ according the Eq. (9), and $\theta_5 = 24.76°$. The corresponding far field scattering is demonstrated in Fig. 15. It can be seen that the scattering angle can be obtained as $\theta_5 = 14°$. The calculation result is in good agreement with the simulation result. Also, S6 = S2 + S3 = 001233112300223011330122..., and the super-period of encoding sequence S6 is τ_{S6} = 24S = 10320 nm. The new encoding metas-

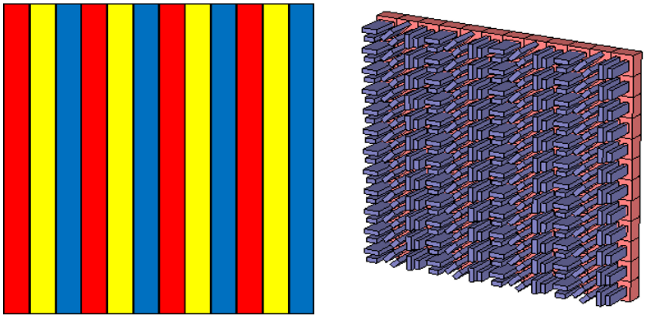

Fig. 14. Arrangement of non-basic sequence S5.

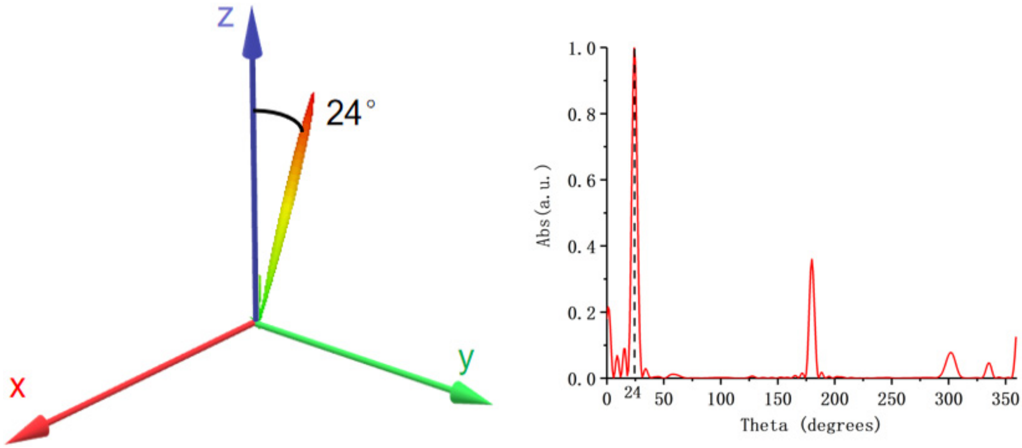

Fig. 15. 3D scattering angle of non-basic sequence S5.

urface sequence S6 can be obtained as shown in Fig. 16. The theoretical scattering angle of θ_6 can be calculated as $\sin\theta_6 = \lambda/8S + \lambda/12S = 0.2618$ according the Eq. (9), and $\theta_6 = 15.18°$. The corresponding far field scattering is demonstrated in Fig. 17. It can be seen that the scattering angle can be obtained as $\theta_6 = 15°$. The two-dimensional

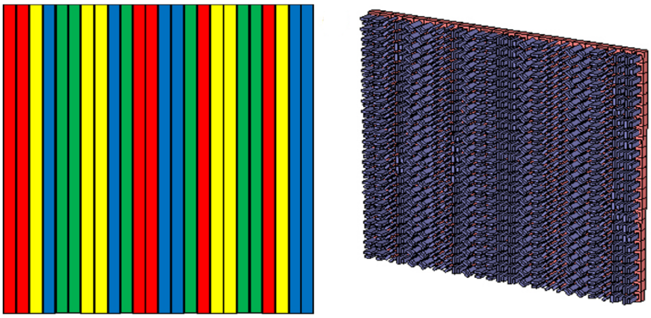

Fig. 16. Arrangement of non-basic sequence S6.

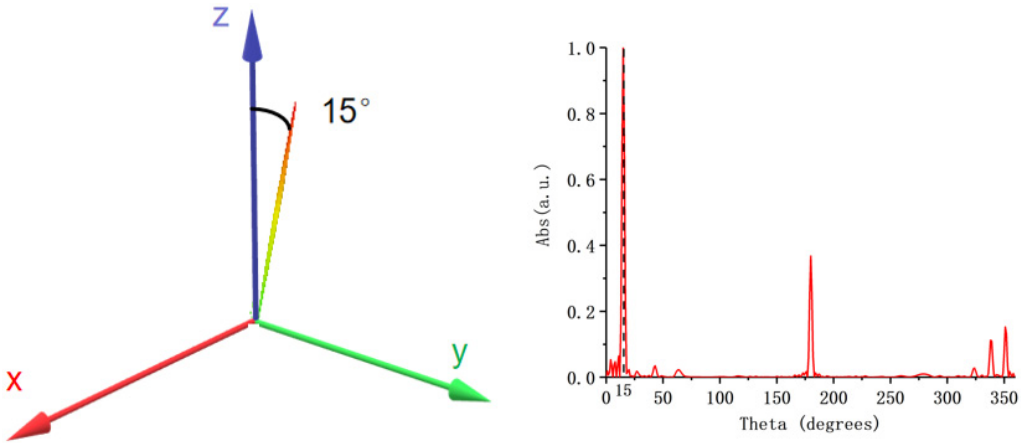

Fig. 17. 3D scattering angle of non-basic sequence S6.

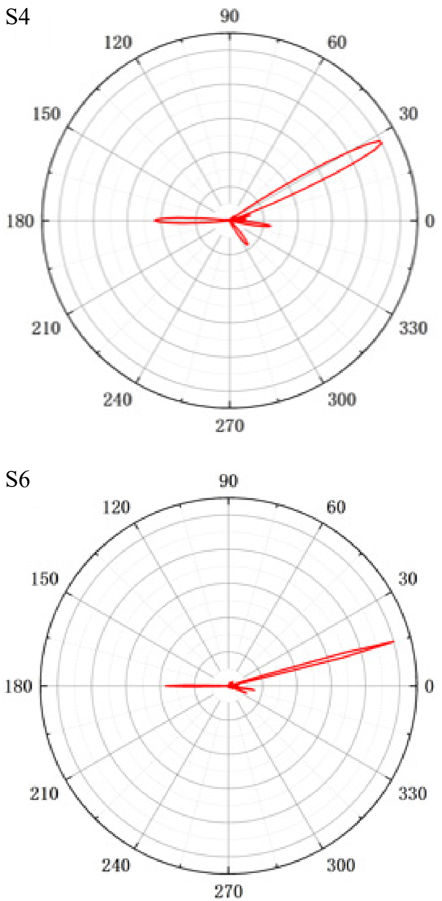

Fig. 18. Polar coordinate diagram of S4, S5, and S6.

circular coordinate scattering pattern corresponding to the three sequences clearly shows the transmission angles corresponding to the different sequences as shown in Fig. 18.

In Eq. (8), a new coding sequence of $f(x_\lambda)\exp(-i\sin\theta_0 x_\lambda)$ can be obtained by subtracting a gradient encoding sequence of $\exp(i\sin\theta_0 x_\lambda)$, where the negative sign in $\exp(-i\sin\theta_0 x_\lambda)$ indicates that it is an opposite sequence to the corresponding sequence of $\exp(i\sin\theta_0 x_\lambda)$. The four-bit operation can be used to the subtraction manipulation of the Fourier convolution principle of Eq. (8) for two gradient encoding sequences. For example, we can subtract the basic sequences to obtain a new non-basic sequence as S7 = S1 – S2 = 30011223.... Here, the negative sign in (S1 – S2) for the sequence S2 indicates the opposite coding sequence. One can understand the new encoding sequence S7 as S7 = S1 + (–S2), and (–S2) can be expressed by (–S2) (3 3 2 2 1 1 0 0...). After the subtraction operation for two encoding metasurface sequences S1 and S2, the new sequence S7 can be demonstrated in Fig. 19. The corresponding far field scattering for S7 is demonstrated in Fig. 20. The scattering angle of S7 can be calculated

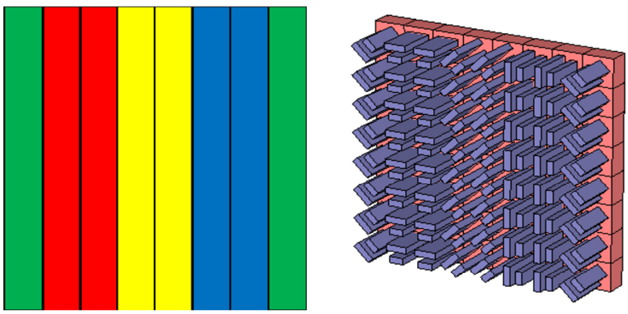

Fig. 19. Arrangement of non-basic sequence S7.

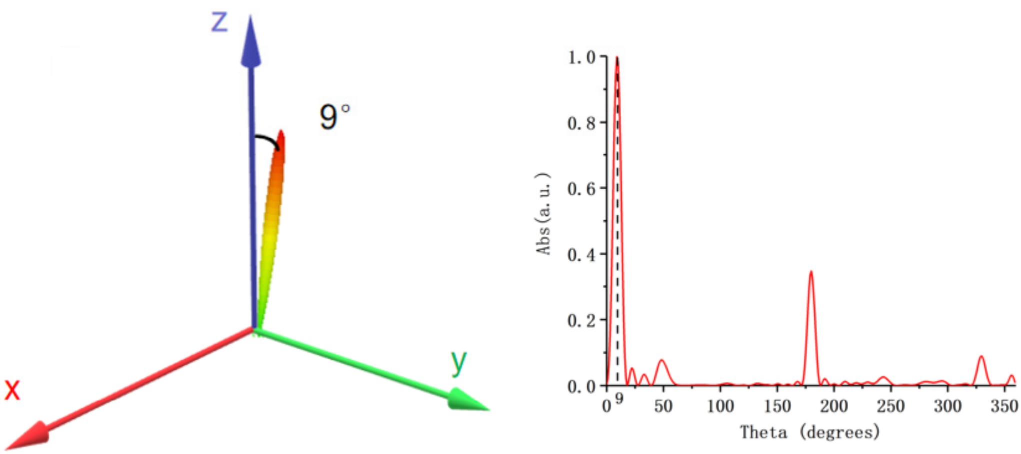

Fig. 20. 3D scattering angle of non-basic sequence S7.

by using $\sin\theta_7 = \lambda/4S + \lambda/8S = 0.1571$, and the angle $\theta_7 = 9.04°$. The numerically simulation scattering angle in Fig. 20 is $\theta_7 = 9°$.

Moreover, a new encoding sequence S8 can be obtained by the subtraction operation from S1 and S3 as S8 = S1 – S3 = 301123.... Figure 21 shows the structural distribution map for S8, and the corresponding far field scattering is shown in Fig. 22. According to $\sin\theta_8 = \lambda/4S + \lambda/12S = 0.2094$, the deflection angle can be obtained as $\theta_8 = 12.09°$. The numerically simulation scattering angle in Fig. 22 is $\theta_8 = 12°$. Similarly, a new encoding sequence S9 can be obtained as S9 = S2 – S3 = = 330300001011112122223233... in Fig. 23. The corresponding far field scattering is shown in Fig. 24. According to $\sin\theta_9 = \lambda/8S - \lambda/12S = 0.0524$, the deflection angle can be obtained as $\theta_9 = 3.00°$. The numerically simulation scattering angle in Fig. 24 is $\theta_9 = 3°$. The calculation results are in good agreement with the simulation results. The two-dimensional circular coordinate scattering pattern corresponding to the three sequences clearly shows the transmission angles corresponding to the different sequences as shown in Fig. 25. These results prove that the subtraction operation of the

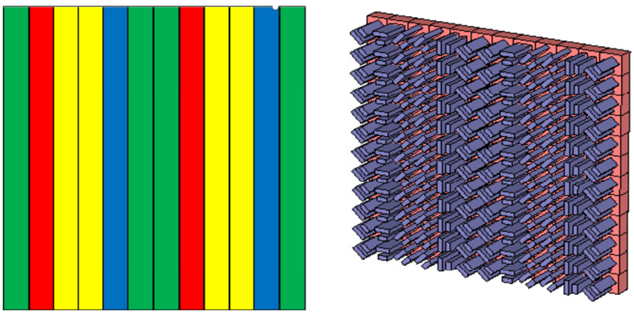

Fig. 21. Arrangement of non-basic sequence S8.

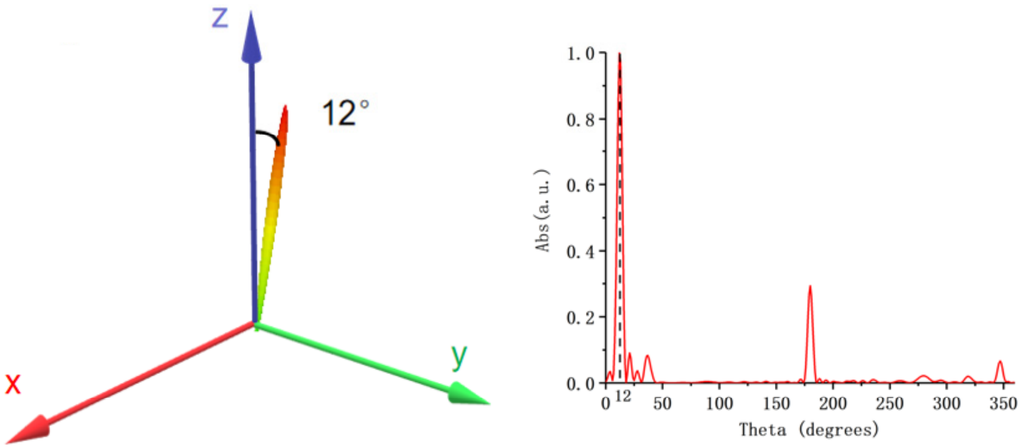

Fig. 22. 3D scattering angle of non-basic sequence S8.

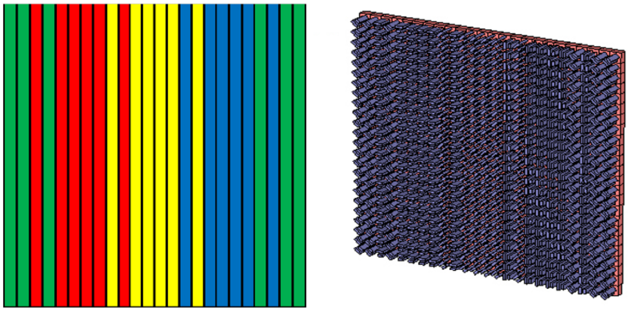

Fig. 23. Arrangement of non-basic sequence S9.

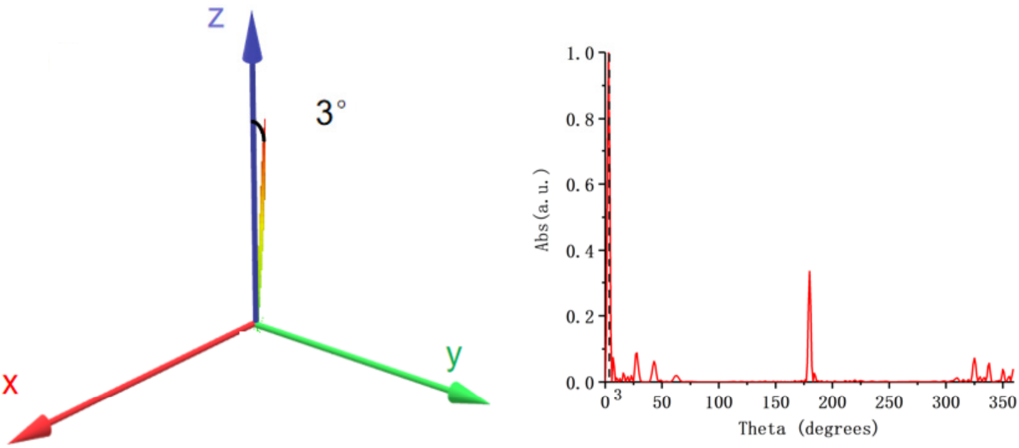

Fig. 24. 3D scattering angle of non-basic sequence S9.

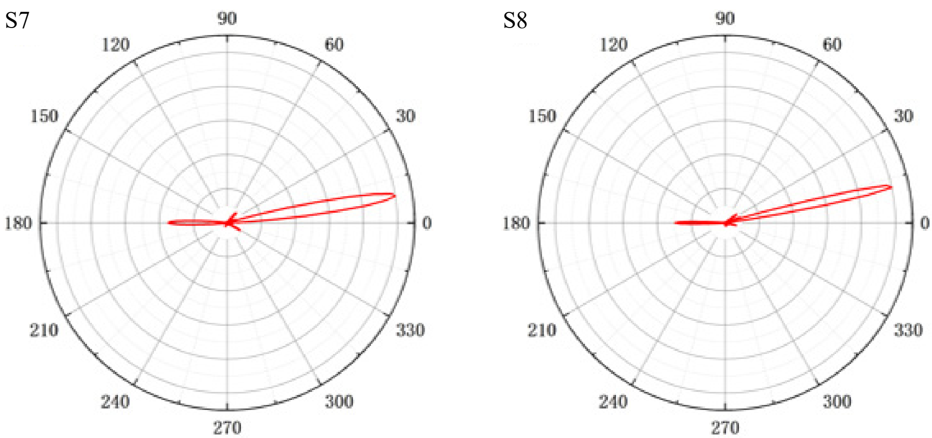

Fig. 25. Polar coordinate diagram of S7, S8, and S9.

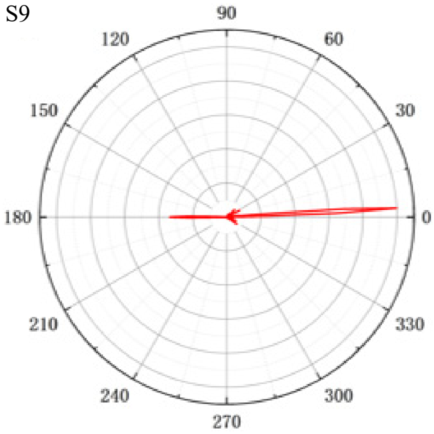

Fig. 25. Continued.

basic sequences also has a certain feasibility on encoding metasurface sequences, and the coded metasurface sequences calculated by subtraction can effectively regulate the scattering characteristics of electromagnetic waves.

Next, we will demonstrate the addition and subtraction of non-base sequences. For example, S10 = S6 + S7 = 3311... and S11 = S6 – S7 = 111333.... Their coding periods are 4S and 6S, respectively. Since these two sequences do not contain 0 and 2 coded particles, even though their periods are integer multiples of the unit structure period, they are still not basic sequences. Figure 26 shows the arrangement of S10, and the encoding sequence S11 is demonstrated in Fig. 27.

Figures 28 and 29 show respectively the far field scattering characteristics of S10 and S11. From their sequence angle diagrams, it can be seen that the scattering angle of S10 is 17° relative to the *z*-axis, while the scattering angle of S11 is 11° relative to the *z*-axis. And they can get two main lobes that are symmetric about the *z*-axis. We can use the principle of coding sequence to explain the reason why 1-bit coding pro-

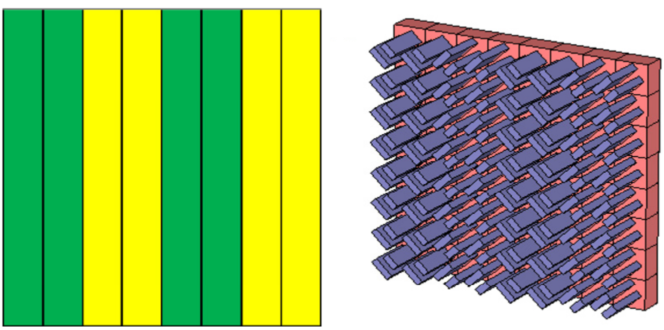

Fig. 26. Arrangement of sequence S10.

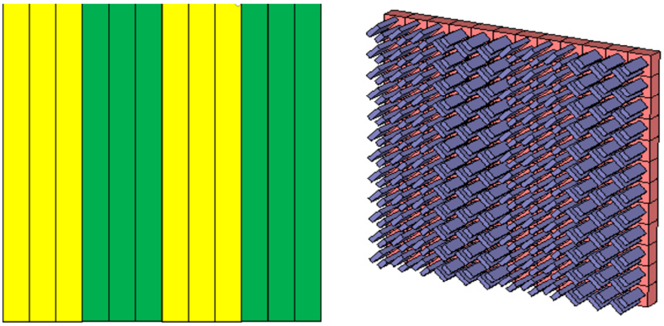

Fig. 27. Arrangement of sequence S11.

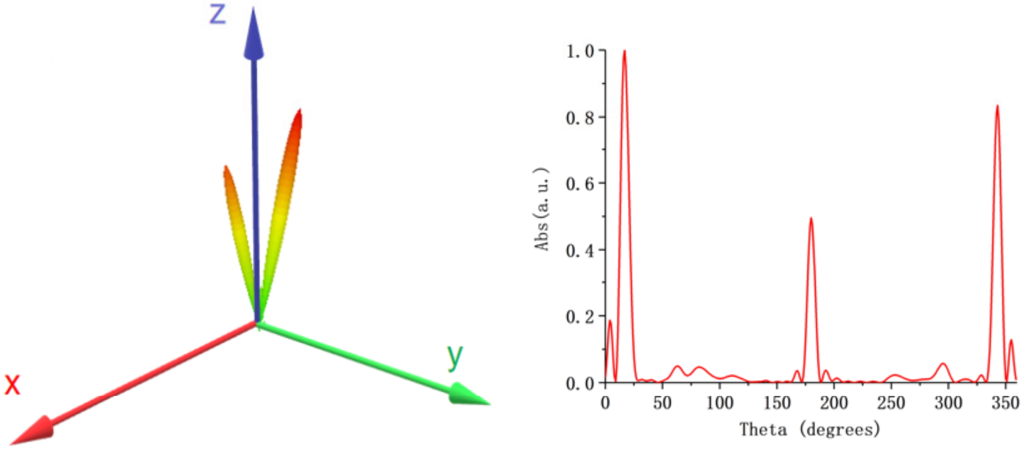

Fig. 28. Scattering angle of S10.

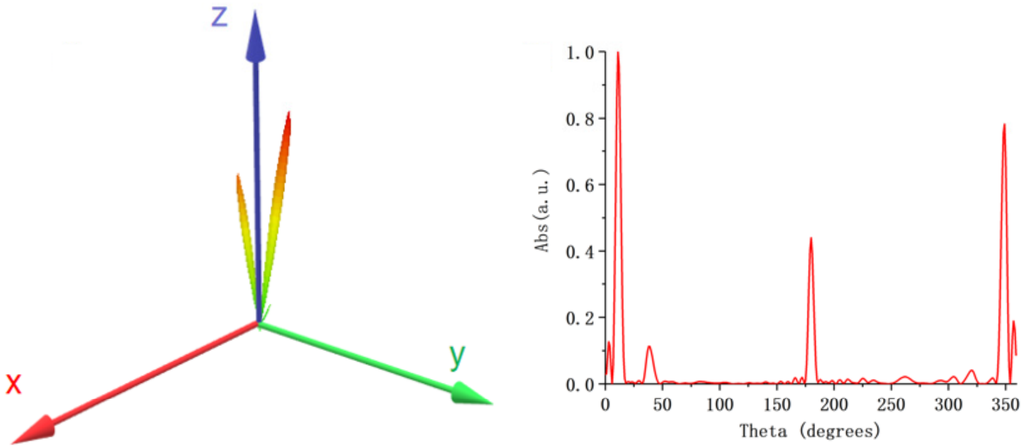

Fig. 29. Figure 28 Scattering angle of S10.

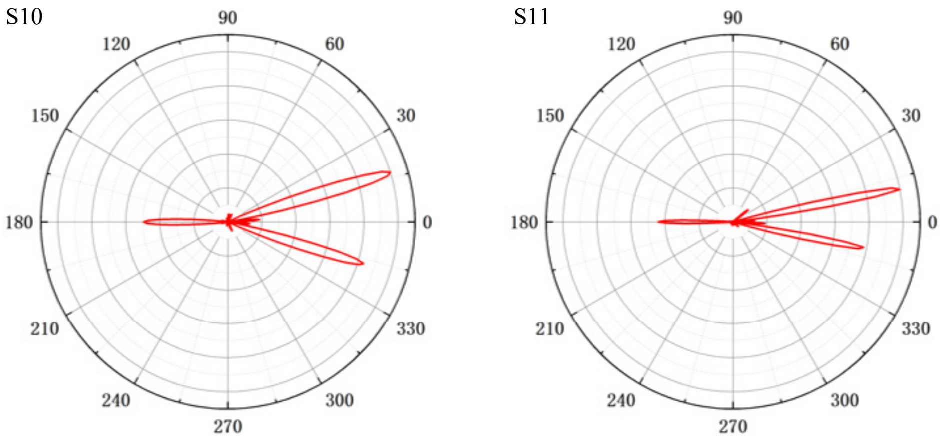

Fig. 30. Polar coordinate diagram of S10 and S11.

duces two main lobes. The two sequences S(1133...) and S(3311...) represent the same metasurface sequences, but their phase gradients are exactly opposite, so their main lobe energy will be equally divided, and they are exactly symmetric about the *z*-axis. The two-dimensional circular coordinate scattering patterns corresponding to the two sequences are demonstrated in Fig. 30. According to the sequence encoding described above, in theory, all the angles of the transmitted light can be controlled. This also illustrates the feasibility of the Fourier convolution principle on the encoding metasurfaces.

6. Fourier convolution of checkerboard encoding metasurfaces

Next, a checkerboard coded metasurface is designed to further prove the characteristics of the Fourier convolution principle on the coded metasurfaces. The period of the coded particles is still 430 nm.We use matrix

$$M = \begin{bmatrix} 0 & 2 \\ 2 & 0 \end{bmatrix} \tag{10}$$

to represent the coding mode of the checkerboard. Each number in the matrix represents 3×3 coded particles. Therefore, the minimum period of the encoded metasurface is $\tau = 6S = 2580$ nm. This checkerboard coded metasurface is on the *xy* plane. In the simulation, the left-handed circularly polarized light (LCP) with a frequency of 555.24 THz is incident on the designed checkerboard coded metasurface. The transmitted scattering angle for the chessboard encoding mode can be calculated according to

$$\theta = \sin^{-1}\left(\frac{\sqrt{2}\,\lambda}{\tau}\right) \tag{11}$$

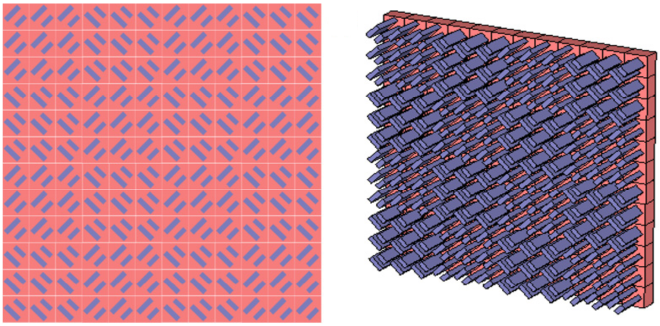

Fig. 31. Arrangement of checkerboard coding metasurface.

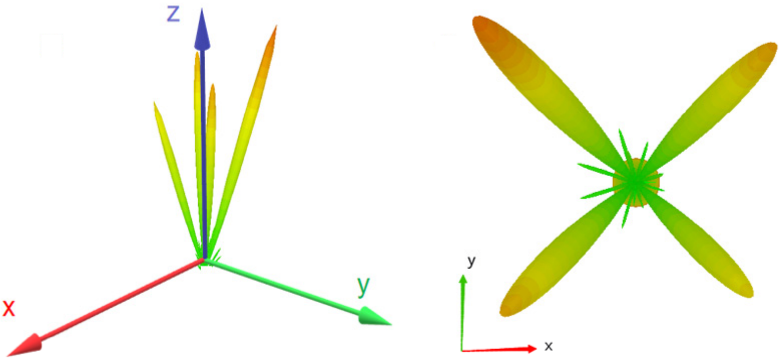

a
b

Fig. 32. Scattering of checkerboard coded metasurface, (**a**) stereo view, (**b**) top view.

In Eq. (11), τ is the size of the checkerboard code's hyperperiod. Figure 31 shows the arrangement of checkerboard coding metasurface. After theoretical calculation in Eq. (11), the transmission angle of the checkerboard encoded metasurface is $\theta = 17.2°$. The specific arrangement of the 12×12 checkerboard coded particles is shown in Fig. 31. The 3D scattering characteristics of metasurface is shown in Fig. 32. The angle of abnormal transmitted light is 16°, which is basically close to the theoretical calculation result. Figure 32 shows a lot of side lobes because the number of overall cell structures calculated is insufficient. When we increase the number of unit particles in calculation, the side lobe of scattering will decrease.

Next, to illustrate the Fourier convolution principle which also applies to checkerboard coded metasurfaces, we select the gradual phase encoding sequence S2 and add it to the checkerboard encoding metasurface M. The mixed encoding sequence can be obtained as S_{MS2} = 001300330233223122112011/223122112011001300330233. The mixed coding sequence is shown in Fig. 33, and the minimum period of this new sequence is 24S. The corresponding transmitted scattering pattern is shown in Fig. 34, and it can be seen that the whole pattern is tilted away from the *z*-direction.

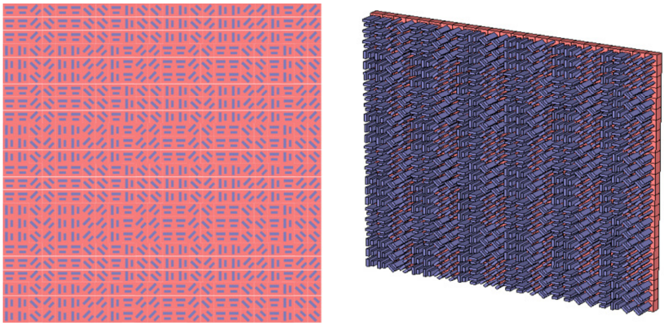

Fig. 33. Schematic and layout diagram of mixed coding sequence.

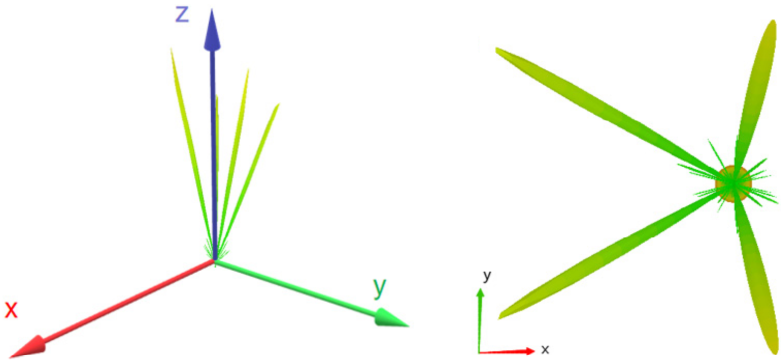

Fig. 34. 3D scatter diagram and top view of mixed coding sequence.

7. Broadband characteristics of encoding metasurfaces

Here, three coding metasurfaces are taken respectively from basic sequence and non-basic sequences to illustrate the bandwidth characteristics of scattering. S1, S4, and S7 were selected to verify the bandwidth of the scattering in the range of 450 to 700 THz. According to Eq. (9), when the incident light with the frequency of 450 THz is incident on the sequence of S1, S4 and S7, the transmission angles were calculated as 22.8°, 35.5°, 11.2°, respectively. When the incident light with the frequency of 700 THz is incident, the transmission angles were calculated as14.4°, 21.9° and 7.2°, respectively. When the incident LCP light with 450 THz is applied, the transmission angle of the encoded metasurface S1 is 22° as shown in Fig. 35, which is in accordance with the theoretical calculation result. When the incident LCP frequency is 700 THz, the transmission angle of the encoded metasurface S1 is 15° in Fig. 36, which is in accordance with the theoretical calculation result.

When the incident LCP frequency is 450 THz, the transmission angle of the encoded metasurface S4 is 35° as shown in Fig. 37, which is in accordance with the theoretical

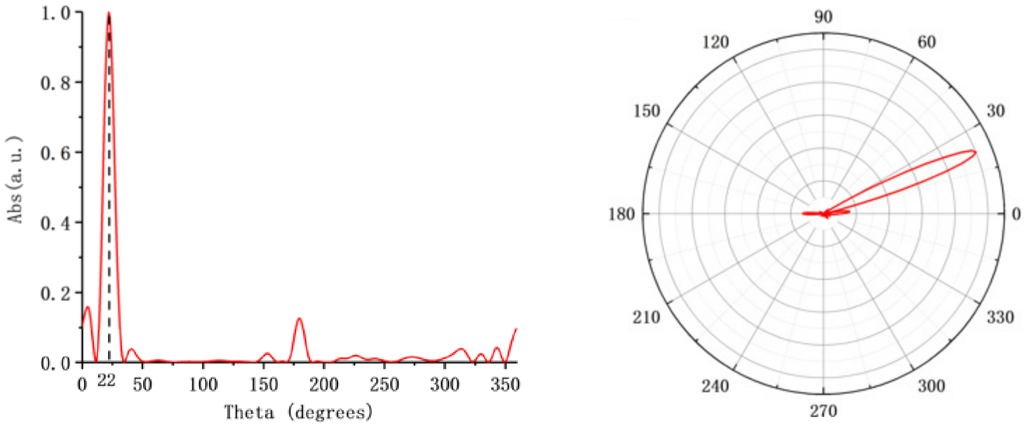

Fig. 35. The scattering results of LCP 450THz incident on S1.

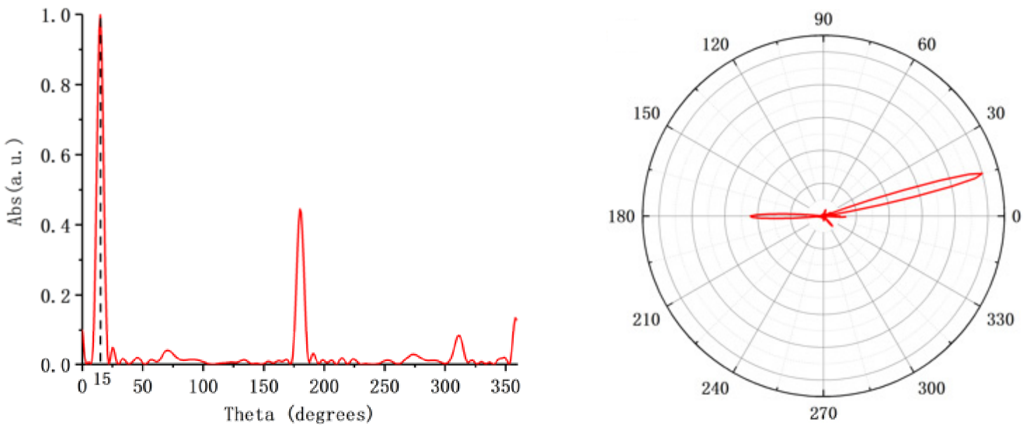

Fig. 36. The scattering results of 700THz LCP incident on S1.

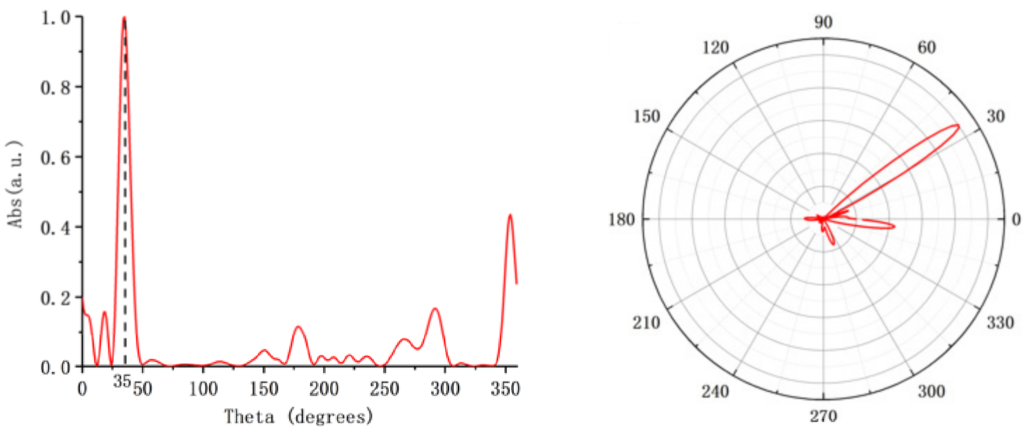

Fig. 37. The scattering results of 450 THz LCP incident on S4.

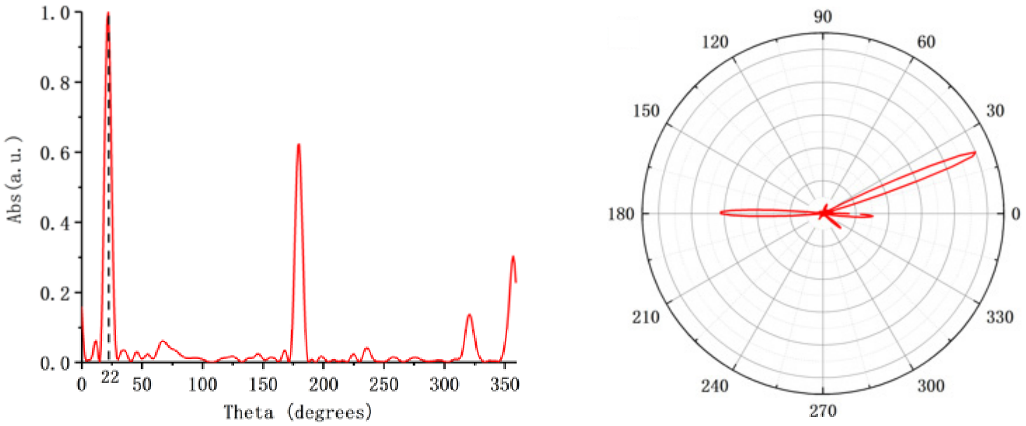

Fig. 38. The scattering results of 700 THz LCP incident on S4.

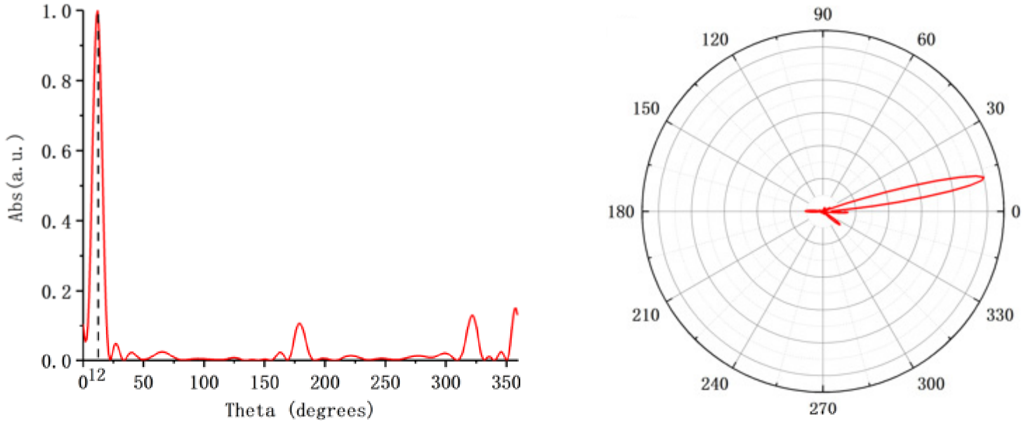

Fig. 39. The scattering results of 450 THz LCP incident on S7.

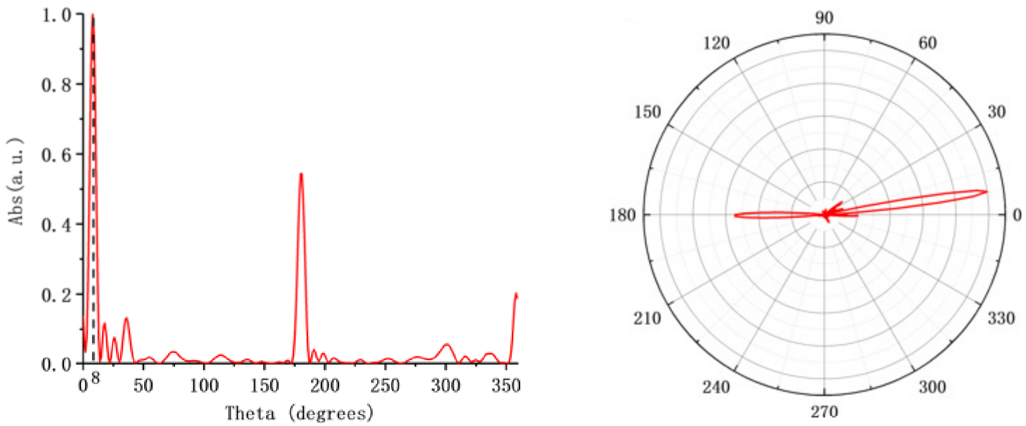

Fig. 40. The scattering results of 700 THz LCP incident on S7.

calculation result. When the incident LCP frequency is 700 THz, the transmission angle of the encoded metasurface S4 is 22° in Fig. 38. When the incident LCP frequency is 450 THz, the transmission angle of the encoded metasurface S7 is 12° in Fig. 39, which is in accordance with the theoretical calculation result. When the incident LCP frequency is 700 THz, the transmission angle of the encoded metasurface S7 is 8° in Fig. 40, which is in accordance with the theoretical calculation result. The broadband characteristics in the range of 450 to 700 THz can be revealed.

Even though the presented work is fully based on numerical simulations of encoding metasurfaces, it is feasible to prepare such all dielectric encoding metasurfaces. Detailed preparation process of all dielectric metasurfaces refers to Ref. [44]. The preparation processes include the base bonding, the conventional mask photolithography, and the Bosch deep reactive ion etching process.

8. Conclusions

In this paper, an all-dielectric material is used on the encoded metasurface to reduce ohmic loss in visible range. In order to obtain the broadband characteristics, we propose a superperiodic structure, that is, two subunit structures are included in a single cell structure. Based on the principle of geometric phase, the transmission phase change within 2π ranges is obtained by rotating the bar structure. Since the basic programming metasurface sequence is only to obtain discrete scattering angles, the continuous angular scattering cannot be realized. We introduce the Fourier convolution principle in digital signal processing. By using the addition and subtraction operations on the two encoding metasurface sequences, a new encoding metasurface sequence can be obtained with different deflection angle. The Fourier convolution principle also applies to the checkerboard encoding scheme. Also, we illustrate the bandwidth characteristics of the proposed encoding metasurface.

Acknowledgement

Natural Science Foundation of Zhejiang Province (No.LZ21A040003, No.LY20F050007); National Natural Science Foundation of China (NSFC) (No. 61875179).

Data availability

The data that support the findings of this study are available from the corresponding author upon a reasonable request.

References

[1] JUNXIANG HUANG, TAO FU, HAIOU LI, ZHAOYU SHOU, XI GAO, *A reconfigurable terahertz polarization converter based on metal–graphene hybrid metasurface*, Chinese Optics Letters **18**(1), 2020, article 013102, DOI: 10.1364/COL.18.013102.

[2] OBULKASIM OLUGH, ZI-LIANG LI, BAI-SONG XIE, *Asymmetric pulse effects on pair production in polarized electric fields*, High Power Laser Science and Engineering **8**(4), 2020, article e38, DOI: 10.1017/hpl.2020.36.

[3] Lin Li, Quan Yuan, Run Chen, Xiujuan Zou, Wenbo Zang, Tianyue Li, Gaige Zheng, Shuming Wang, Zhenlin Wang, Shining Zhu, *Chromatic dispersion manipulation based on metasurface devices in the mid-infrared region*, Chinese Optics Letters **18**(8), 2020, article 082401, DOI: 10.1364/COL.18.082401.

[4] Shuyun Teng, Qi Zhang, Han Wang, Lixia Liu, Haoran Lv, *Conversion between polarization states based on metasurface*, Photonics Research **7**(3), 2019, pp. 246–250, DOI: 10.1364/PRJ.7.000246.

[5] He X., Lu H., *Graphene-supported tunable extraordinary transmission*, Nanotechnology **25**(32), 2014, article 325201, DOI: 10.1088/0957-4484/25/32/325201.

[6] He X., *Tunable terahertz graphene metamaterials*, Carbon **82**, 2015, pp. 229–237, DOI: 10.1016/j.carbon.2014.10.066.

[7] Guan H., Chen H., Wu J., Jin Y., Kong F., Liu S., Yi K., Shao J., *High-efficiency, broad-bandwidth metal/multilayer-dielectric gratings*, Optics Letters **39**(1), 2014, pp. 170–173, DOI: 10.1364/OL.39.000170.

[8] He X., Zhong X., Lin F., Shi W., *Investigation of graphene assisted tunable terahertz metamaterials absorber*, Optical Materials Express **6**(2), 2016, pp. 331–342, DOI: 10.1364/OME.6.000331.

[9] Akram M.R., Ding G., Chen K., Feng Y., Zhu W., *Ultrathin single layer metasurfaces with ultra-wideband operation for both transmission and reflection*, Advanced Materials **32**(12), 2020, article 1907308, DOI: 10.1002/adma.201907308.

[10] Akram M.R., Mehmood M.Q., Bai X., Jin R., Premaratne M., Zhu W., *High efficiency ultrathin transmissive metasurfaces*, Advanced Optical Materials **7**(11), 2019, article 1801628, DOI: 10.1002/adom.201801628.

[11] Junyu Xiao, Ruiwen Xiao, Rongxuan Zhang, Zhixiong Shen, Wei Hu, Lei Wang, Yanqing Lu, *Tunable terahertz absorber based on transparent and flexible metamaterial*, Chinese Optics Letters **18**(9), 2020, article 092403, DOI: 10.1364/COL.18.092403.

[12] Lei Xia, Yuanzhang Hu, Wenyu Chen, Xiaoguang Li, *Decoupling of the position and angular errors in laser pointing with a neural network method*, High Power Laser Science and Engineering **8**(3), 2020, article e28, DOI: 10.1017/hpl.2020.29.

[13] Fei Ding, Yiting Chen, Bozhevolnyi S.I., *Gap-surface plasmon metasurfaces for linear-polarization conversion, focusing, and beam splitting*, Photonics Research **8**(5), 2020, pp. 707–714, DOI: 10.1364/PRJ.386655.

[14] Hornung J., Zobus Y., Boller P., Brabetz C., Eisenbarth U., Kühl T., Major Zs., Ohland J.B., Zepf M., Zielbauer B., Bagnoud V., *Enhancement of the laser-driven proton source at PHELIX*, High Power Laser Science and Engineering **8**(2), 2020, article 02000e24, DOI: 10.1017/hpl.2020.23.

[15] Akram M., Bai X., Jin R., Vandenbosch G., Premaratne M., Zhu W., *Photon spin Hall effect-based ultra-thin transmissive metasurface for efficient generation of OAM waves*, IEEE Transactions on Antennas and Propagation **67**(7), 2019, pp. 4650–4658, DOI: 10.1109/TAP.2019.2905777.

[16] Haoran Lv, Xiaoqing Lu, Yuansheng Han, Zhen Mou, Changda Zhou, Shuyun Wang, Shuyun Teng, *Metasurface cylindrical vector light generators based on nanometer holes*, New Journal of Physics **21**, 2019, article 123047, DOI: 10.1088/1367-2630/ab5f44.

[17] Han Wang, Lixia Liu, Changda Zhou, Jilian Xu, Meina Zhang, Shuyun Teng, Yangjian Cai, *Vortex beam generation with variable topological charge based on a spiral slit*, Nanophotonics **8**(2), 2019, pp. 317–324, DOI: 10.1515/nanoph-2018-0214.

[18] Qi Zhang, Han Wang, Lixia Liu, Shuyun Teng, *Generation of vector beams using spatial variation nanoslits with linearly polarized light illumination*, Optics Express **26**(18), 2018, pp. 24145–24153, DOI: 10.1364/OE.26.024145.

[19] Han Wang, Lixia Liu, Chunxiang Liu, Xing Li, Shuyun Wang, Qing Xu, Shuyun Teng, *Plasmonic vortex generator without polarization dependence*, New Journal of Physics **20**, 2018, article 033024, DOI: 10.1088/1367-2630/aaafbb.

[20] Lamprou T., Liontos I., Papadakis N., Tzallas P., *A perspective on high photon flux nonclassical light and applications in nonlinear optics*, High Power Laser Science and Engineering **8**, 2020, article e42, DOI: 10.1017/hpl.2020.44.

[21] Fu Y.Y., Xu Y.D., Chen H.Y., *Negative refraction based on purely imaginary metamaterials*, Frontiers of Physics **13**(4), 2018, article 134206, DOI: 10.1007/s11467-018-0781-3.
[22] He Z.Z., Zhu Y.B., Wu H.A., *Self-folding mechanics of graphene tearing and peeling from a substrate*, Frontiers of Physics **13**(3), 2018, article 138111, DOI: 10.1007/s11467-018-0755-5.
[23] Rubin S., Fainman Y., *Nonlinear, tunable, and active optical metasurface with liquid film*, Advanced Photonics **1**(6), 2019, article 066003, DOI: 10.1117/1.AP.1.6.066003.
[24] Song Z.Y., Chu Q.Q., Shen X.P., Liu Q.H., *Wideband high-efficient linear polarization rotators*, Frontiers of Physics **13**(5), 2018, article 137803, DOI: 10.1007/s11467-018-0779-x.
[25] Zhao W., Chu H., Tao Z., Hang Z.H., *Acoustic transmissive cloaking using zero-index materials and metasurfaces*, Applied Physics Express **12**(5), 2019, article 054004, DOI: 10.7567/1882-0786/ab14ad.
[26] Cui T.J., Qi M.Q., Wan X., Zhao J., Cheng Q., *Coding metamaterials, digital metamaterials and programmable metamaterials*, Light: Science & Applications **3**(10), 2014, article e218, DOI: 10.1038/lsa.2014.99.
[27] Hu Z, Xu T., Tang R., Guo H.J., Xiao S.Y., *Geometric-phase metasurfaces: from physics to applications*, Laser & Optoelectronics Progress **56**(20), 2019, pp. 113–133.
[28] He X., Zhong X., Lin F., Shi W., *Investigation of graphene assisted tunable terahertz metamaterials absorber*, Optical Materials Express **6**(2), 2016, pp. 331–342, DOI: 10.1364/OME.6.000331.
[29] Bo Fang, Zhiyu Cai, Yandong Peng, Chenxia Li, Zhi Hong, Xufeng Jing, *Realization of ultrahigh refractive index in terahertz region by multiple layers coupled metal ring metamaterials*, Journal of Electromagnetic Waves and Applications **33**(11), 2019, pp. 1375–1390, DOI: 10.1080/09205071.2019.1608868.
[30] Fang B., Li B., Peng Y., Li C., Hong Z., Jing X., *Polarization-independent multiband metamaterials absorber by fundamental cavity mode of multilayer microstructure*, Microwave and Optical Technology Letters **61**(10), 2019, pp. 2385–2391, DOI: 10.1002/mop.31890.
[31] Weimin Wang, Xufeng Jing, Jingyin Zhao, Yinyan Li, Ying Tian, *Improvement of accuracy of simple methods for design and analysis of a blazed phase grating microstructure*, Optica Applicata **47**(2), 2017, pp. 183–198, DOI: 10.5277/oa170202.
[32] Jiang L., Fang B., Yan Z., Li C., Fu J., Gan H., Hong Z., Jing X., *Improvement of unidirectional scattering characteristics based on multiple nanospheres array*, Microwave and Optical Technology Letters **62**(6), 2020, pp. 2405–2414, DOI: 10.1002/mop.32328.
[33] Jing X., Gui X., Zhou P., Hong Z., *Physical explanation of Fabry–Pérot cavity for broadband bilayer metamaterials polarization converter*, Journal of Lightwave Technology **36**(12), 2018, pp. 2322–2327, DOI: 10.1109/JLT.2018.2808339.
[34] Xia R., Jing X., Gui X., Tian Y., Hong Z., *Broadband terahertz half-wave plate based on anisotropic polarization conversion metamaterials*, Optical Materials Express **7**(3), 2017, pp. 977–988, DOI: 10.1364/OME.7.000977.
[35] Zhao J., Jing X., Wang W., Tian Y., Zhu D., Shi G., *Steady method to retrieve effective electromagnetic parameters of bianisotropic metamaterials at one incident direction in the terahertz region*, Optics & Laser Technology **95**, 2017, pp. 56–62, DOI: 10.1016/j.optlastec.2017.04.001.
[36] Tian Y., Jing X., Gan H., Li C., Hong Z., *Free control of far-field scattering angle of transmission terahertz wave using multilayer split-ring resonators' metasurfaces*, Frontiers of Physics **15**, 2020, article 62502, DOI: 10.1007/s11467-020-1013-1.
[37] Jing X., Jin S., Tian Y., Liang P., Dong Q., Wang L., *Analysis of the sinusoidal nanopatterning grating structure*, Optics & Laser Technology **48**, 2013, pp. 160–166, DOI: 10.1016/j.optlastec.2012.10.008.
[38] Jing X., Xu Y., Gan H., He Y., Hong Z., *High refractive index metamaterials by using higher order modes resonances of hollow cylindrical nanostructure in visible region*, IEEE Access **7**, 2019, pp. 144945–144956, DOI: 10.1109/ACCESS.2019.2945119.

[39] JIANG L., FANG B., YAN Z., FAN J., QI C., LIU J., HE Y., LI C., JING X., GAN H., HONG Z., *Terahertz high and near-zero refractive index metamaterials by double layer metal ring microstructure*, Optics & Laser Technology **123**, 2020, article 105949, DOI: 10.1016/j.optlastec.2019.105949.

[40] RUIQI MAO, GUANGMING WANG, TONG CAI, KAIYUE LIU, DENGPAN WANG, BORUI WU, *Ultra-thin and high-efficiency full-space Pancharatnam–Berry metasurface*, Optics Express **28**(21), 2020, pp. 31216–31225, DOI: 10.1364/OE.405086.

[41] XU H.X., WANG G.M., CAI T., XIAO J., ZHUANG Y.Q., *Tunable Pancharatnam–Berry metasurface for dynamical and high-efficiency anomalous reflection*, Optics Express **24**(24), 2016, pp. 27836–27848, DOI: 10.1364/OE.24.027836.

[42] SHAO L., PREMARATNE M., ZHU W.R., *Dual-functional coding metasurfaces made of anisotropic all-dielectric resonators*, IEEE Access **7**, 2019, pp. 45716–45722, DOI: 10.1109/ACCESS.2019.2908830.

[43] YU N.F., GENEVET P., KATS M.A., AIETA F., TETIENNE J.P., CAPASSO F., GABURRO Z., *Light propagation with phase discontinuities: generalized laws of reflection and refraction*, Science **334**(6054), 2011, pp. 333–337, DOI: 10.1126/science.1210713.

[44] MA Z., HANHAM S., ALBELLA P., NG B., LU H., GONG Y., MAIER S., HONG M., *Terahertz all-dielectric magnetic mirror metasurfaces*, ACS Photonics **3**(6), 2016, pp. 1010–1018, DOI: 10.1021/acsphotonics.6b00096.

Received March 26, 2021
in revised form May 14, 2021